Al matrix composites reinforced by in situ synthesized graphene–Cu hybrid layers: interface control by spark plasma sintering conditions

Bowen Pu, David Mesguich, Claude Estournès, Xiang Zhang, Geoffroy Chevallier, Naiqin Zhao, Christophe Laurent

Al matrix composites reinforced by *in situ* synthesized graphene–Cu hybrid layers: interface control by spark plasma sintering conditions

Bowen Pu[1], David Mesguich[2], Claude Estournès[2], Xiang Zhang[1], Geoffroy Chevallier[2], Naiqin Zhao[1,3,*], and Christophe Laurent[2,*]

[1] School of Materials Science and Engineering and Tianjin Key Laboratory of Composite and Functional Materials, Tianjin University, Tianjin 300350, People's Republic of China

[2] CIRIMAT, CNRS-INP-UPS, Université Toulouse 3 Paul Sabatier, 118 Route de Narbonne, 31062, Toulouse, Cedex 9, France

[3] Key Laboratory of Advanced Ceramics and Machining Technology, Ministry of Education, Tianjin University, Tianjin 300072, People's Republic of China

ABSTRACT

Tremendous impacts are usually made by the synthesis method and consolidation technique on microstructure and interface of graphene/Al composites. In the present work, an in situ gel-precursor decomposition route is proposed for the one-step synthesis of graphene nanosheet (GNS) decorated with Cu nanoparticles in the form of hybrid layers encapsulating Al grains (designated as GNS–Cu/Al). Consolidation is performed by spark plasma sintering (SPS) using markedly different sets of maximum temperature and maximum uniaxial pressure (400 °C/400 MPa or 500 °C/100 MPa). The powder and dense samples are investigated by several techniques including thermal analysis, X-ray diffraction and electron microscopy. The microhardness and elastic modulus of selected GNS–Cu/Al composites are investigated and related to the microstructure and preparation conditions. Results demonstrate that the interface structure is primarily determined by the roles of GNS–Cu hybrid layers and finely controlled by SPS conditions. This work paves a novel way to elucidate the evolutions of metal-decorated graphene hybrids in Al matrix composites.

Address correspondence to E-mail: nqzhao@tju.edu.cn; christophe.laurent@univ-tlse3.fr

https://doi.org/10.1007/s10853-022-07057-3

GRAPHICAL ABSTRACT

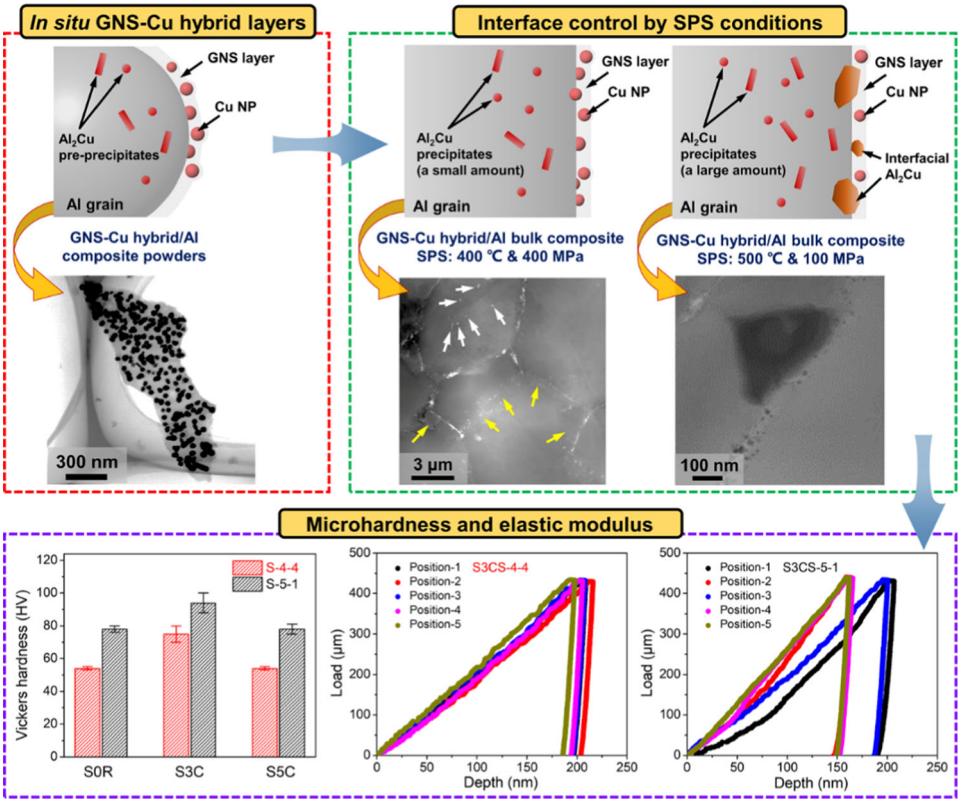

Introduction

Graphene [1] has drawn a surge of interest for the reinforcement of advanced metal matrix composites, including aluminum matrix composites [2–4]. It is important to note that the undesirably irreversible agglomeration of graphene in the sample, because of processing issues, and its weak interfacial bonding with the Al matrix both result in lower mechanical reinforcement effect than theoretically expected [5]. Extensive research has been reported in the past decade on the dispersion of graphene and on graphene/Al interface optimization, involving powder metallurgy routes [6–11] and post-treatments of bulk composites [12–15]. Remarkable breakthroughs have been achieved in the strengthening efficiency of graphene-reinforced Al matrix composites. Interfacial second phases (i.e., other than graphene) such as Al_4C_3 can be formed in situ and ensure a covalent bonding with the graphene [16–19], providing some interfacial interlocking and generating some reinforcing. However, an excessive amount of such nanosized carbides deteriorates the interface strength [20, 21]. In addition, decorating the graphene by precoating metal or ceramic particles will also increase the interfacial bonding in graphene/Al composites [22–24]. However, shortcomings of routes complexity and impurity introduction are usually associated with this method, which limits its practical application. The above-mentioned research mainly adopted ex situ preparation processes by relatively complicated routes, while limited investigation on the intrinsic synthesis strategy of graphene/Al composite powders was carried out.

In order to simultaneously realize a uniform dispersion of graphene and a strong interfacial bonding, in situ thermal decomposition of carbon sources is a promising way to directly form nanocarbons on metal surfaces [25]. As an intrinsic one-step synthesis strategy assisted by catalysts and their reaction with carbon atoms, it has three unique advantages, which include: (i) the well-defined interface structure between nanocarbon and metal matrix by tuning experimental parameters [26], (ii) the maintained structural integrity of nanocarbon within the composites by obviating the chemical modification step [27], (iii) the homogeneous dispersion of nanocarbon on premise of uniform dispersion of catalyst [28]. Both the decomposition of carbon sources and the growth of graphene are deeply affected by the temperature and the active catalyst surfaces. Due to the low melting point and passivated surfaces of Al, in situ synthesis of graphene on Al grains is difficult to achieve without metal catalysts, which is notably different from the formation mechanisms of graphene on Cu, Ni or ceramic grains [29–32]. Inspired by the works of Lee et al. [33], the agglomeration of Cu nanoparticles during the high-temperature annealing process was resolved by using a solid carbon source to replace the gas one. Indeed, Wang et al. [34] proposed a versatile fabrication method of multilayered graphene on the surface of Cu nanoparticles via metal–organic chemical vapor deposition (CVD), involving the decomposition of precursors containing both Cu and C atoms at 600 °C. In our previous studies [35–38], three-dimensional graphene modified with some catalytic metal nanoparticles (e.g., Cu, Ni, Sn, etc.) was prepared by decomposing the solid carbon source on templates of sodium chloride crystal. Even so, the use of the decomposition of a solid carbon source directly on an Al powder bed for the synthesis optimization of graphene/Al composites has hitherto not been investigated. Herein, an innovative technique of in situ gel-precursor decomposition was developed for the one-step synthesis of graphene nanosheets (GNS) decorated with Cu nanoparticles to encapsulate Al grains (designated as GNS–Cu/Al). The Cu nanoparticles serve as both the catalyst for the synthesis of GNS [39] and the modification for the GNS–Al interface.

The consolidation technique and its parameter selections make a tremendous impact on the microstructures of graphene/Al composites. Spark plasma sintering (SPS) has been used extensively because it is relatively fast [40]. Earlier works [41, 42] have shown that controlling the interfacial phases (i.e., located at the grain boundaries of the Al matrix) will considerably affect the interfacial shear strength, hence the mechanical properties of the composites. Conventional sintering for metal-decorated graphene/Al composites is prone to produce Al_4C_3 and intermetallic compounds at the same time but the interactions among multiple interfacial products are often complicated and it is hard to clarify their respective roles. Attention has rarely been paid yet to the fact that the metal decoration in graphene can preferentially form the intermetallic compound before the temperature of Al_4C_3 formation. The aim of the present work is to investigate how different SPS parameters (maximum temperature and maximum uniaxial pressure) can lead to the densification of the samples composite with the formation of intermetallic compounds at the grain boundaries while avoiding the formation of Al_4C_3. The microhardness and elastic modulus of the GNS–Cu/Al composites are investigated.

Experimental

In situ synthesis of GNS–Cu/Al composite powders

Al powders (99.5%, irregular spherical morphology, diameter 16 ± 8 μm), anhydrous glucose ($C_6H_{12}O_6$) and $Cu(NO_3)_2{\cdot}3H_2O$ were purchased from Alfa Aesar Company. The preparation process of GNS–Cu/Al composites is illustrated in Fig. 1. Specifically, 10 g of Al powder were added into an aqueous solution containing 1.699 g of $Cu(NO_3)_2{\cdot}3H_2O$, from 0 up to 3.0 g of $C_6H_{12}O_6$ and 12 mL of distilled water (Fig. 1a). The $C_6H_{12}O_6$ content was varied in order to control the carbon content in the final samples (Table 1). The Al powder was completely soaked in the solution. The so-obtained suspension was rapidly frozen in liquid nitrogen and the sample was freeze-dried (Christ alpha 2–4 LD, Bioblock Scientific, −40 °C, 12 Pa, 48 h), producing dry gels (Fig. 1b), denoted as S0–S6 hereafter. The gels were placed in a horizontal tube furnace and calcined in argon (Ar) up to 600 °C (heating rate 600 °C/h), where hydrogen (H_2) was introduced (Ar/H_2, 200/100 mL/min) for a dwell time of 1 h, provoking the decomposition of

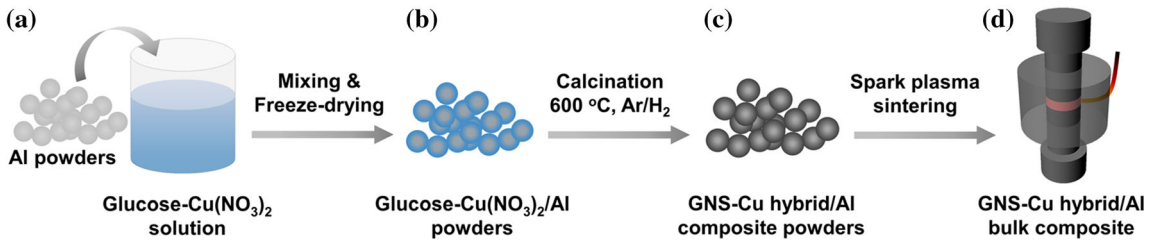

Figure 1 Schematic illustrations for the fabrication process of GNS Cu/Al composites.

Table 1 Experimental and theoretical copper and carbon contents in the powders

Sample	Initial Cu/Al ratio (wt%)	Theoretical Cu content (wt%)	Initial glucose/Al ratio (wt%)	Theoretical C content (wt%)	Experimental C content (wt%)
S0 (S0R & S0C)	4.50	4.31	0	0	0
S1 (S1C)	4.50	4.29	1.25	0.48	0.06
S2 (S2C)	4.50	4.27	2.50	0.95	0.13
S3 (S3C)	4.50	4.23	5.00	1.88	0.22
S4 (S4C)	4.50	4.19	7.50	2.79	0.32
S5 (S5C)	4.50	4.07	15.00	5.43	1.77
S6 (S6C)	4.50	3.86	30.00	10.30	2.78

the glucose and copper nitrate and therefore producing GNS–Cu/Al composite powders (Fig. 1c). The samples are denoted as S0C–S6C hereafter. (Of course, here GNS content is nil for S0C.) S0 (no added $C_6H_{12}O_6$) was also heated in pure H_2 (200 mL/min) at only 300 °C (heating rate 300 °C/h, dwell time 1 h) to obtain a carbon-free sample (denoted as S0R hereafter), for the sake of comparison with S0C.

Consolidation of the GNS–Cu/Al composites

The SPS system (FUJI 632Lx) was used to consolidate the composite powders (Fig. 1d). The compacts were prepared in a WC–Co die (Pedersen, WC–Co 93.5: 6.5 wt%). Prior to the introduction of the powder in the die, a graphitic foil (Perma-Foil®, Toyo Tanso) was placed between punches and die and between die and powder to allow for an easy removal after sintering. The SPS cycles are illustrated in Fig. 2. A pre-

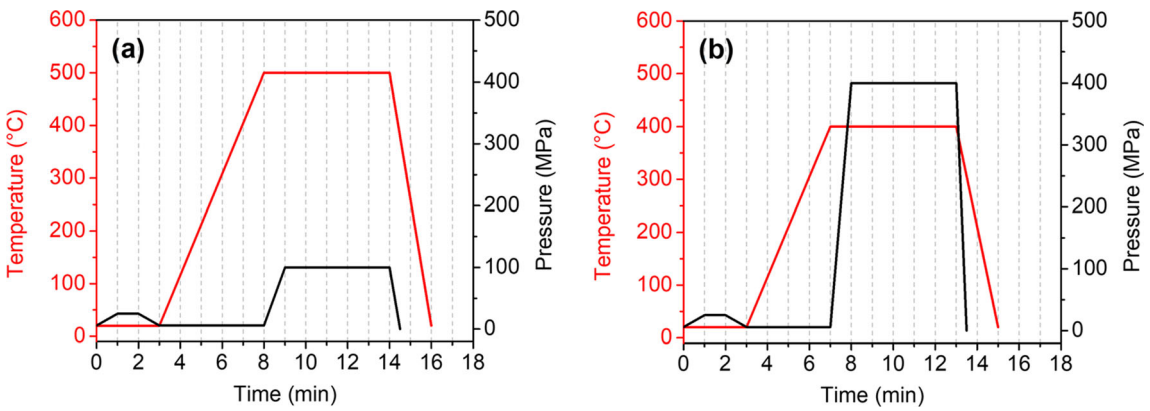

Figure 2 Spark plasma sintering cycles: **a** 500 °C and 100 MPa (conditions S 5 1) and **b** 400 °C and 400 MPa (conditions S 4 4).

compaction step (25 MPa, 1 min) was performed at room temperature in order to give all the samples the same initial compact relative density. The SPS run was performed in vacuum (residual cell pressure below 5 Pa) using a pulsed current pattern of 40 ms: 7 ms (pulse on: pulse off). A heating rate of 100 °C/min was used to reach the maximum temperature (either 400 or 500 °C), where a dwell time of 5 min was applied. The uniaxial pressure (either 100 or 400 MPa), was applied during the first minute of the dwell. The combinations of 500 °C with 100 MPa (denoted as S-5-1) (Fig. 2a) and 400 °C with 400 MPa (denoted as S-4-4) (Fig. 2b) were selected. The pellets show a final diameter of 8 mm and a final thickness of 2 mm.

Characterization

The experimental carbon content in the S1C−S6C powders was evaluated by a CHNS/O elemental analysis (PerkinElmer-2400 series II) based on the classical Pregl–Dumas technique (flash combustion). The thermal behavior of $C_6H_{12}O_6$ and $Cu(NO_3)_2$-$3H_2O$ were investigated using simultaneous thermogravimetric analysis (TGA) and differential thermal analysis (DTA) (Setsys Evo, Setaram thermoanalyzer) from room temperature to 600 °C with a heating rate of 2 °C/min in Ar or H_2 gas atmosphere. The X-ray diffraction (XRD) patterns of the powders and sintered samples were recorded using a Bruker D4 diffractometer using Cu Kα radiation. Raman spectra of the S1C–S6C powders were recorded using a Renishaw inVia Microscope (532-nm laser). The powders were observed by scanning electron microscopy (SEM, VEGA3-TESCAN) using backscattered electron (BSE) imaging mode. Selected powders and sintered samples were observed by transmission electron microscopy (TEM, JEOL JEM-2100F), which included the regular TEM observation, high-resolution transmission electron microscopy (HRTEM), bright-field (BF) scanning TEM (STEM), high-angle annular dark-field (HAADF) STEM and energy dispersive spectrometry (EDS). The TEM samples (∼ 3 mm in diameter) were prepared by polishing and ion-milling (Gatan-PIPS695). The apparent density of the compacts was measured by Archimedes' principle using a hydrostatic balance (Sartorius MSE224S-YDK03), and the values reported are the average of 12 tests. Microhardness tests were conducted with a 0.1 kg load and 10 s dwell time (Mitutoyo, HM-200), and the values reported are the average of ten tests. The error bars correspond to the standard deviations (± SD) of the results. Nanoindentation was performed with a Berkovich pyramid-shaped diamond tip (Hysitron TI-Premier Corp., Eden Prairie, MN, USA), in order to determine the elastic modulus and hardness. It was operated to the maximum load of 430 μN applied within 5 s and held for 2 s at peak load.

Results and discussion

Powders

The experimental carbon content increases upon the increase in the initial glucose/Al ratio, but it is only about 30% of the theoretical carbon content expected assuming $C_6H_{12}O_6$ completely decomposes without any carbon loss (Fig. 3 and Table 1). A linear relation was found (Fig. 3b), which could provide a reference for the quantitative design of composition of future samples. However, the decomposition of the copper nitrate in Ar/H_2 gas atmosphere may affect the decomposition of $C_6H_{12}O_6$ as discussed below.

The TG and DTA curves in Ar gas for $C_6H_{12}O_6$ (Fig. 4a) first show a weight loss of about 20% accompanied by two endothermic peaks (153 °C, stage A and 191 °C, stage B), corresponding to the melting and partial dehydration of $C_6H_{12}O_6$, respectively. Then, a marked weight loss (191−350 °C) accompanied by an exothermic peak (301 °C, stage C) is followed (350–600 °C) by a more progressive weight loss, corresponding to the decomposition and carbonization of $C_6H_{12}O_6$. This can be described as $C_6H_{12}O_{6\ (s)} \rightarrow 6\ C_{\ (s)} + 6\ H_2O_{\ (g)}$, with a theoretical weight loss equal to 60%. However, the sample underwent an excessive weight loss (∼ 78.2%) up to 600 °C. This could correspond to progressive carbon volatilization because of the exothermic heat flow during stage C. Indeed, the latter (Fig. 4b) shows, in Ar gas atmosphere, successive weight losses accompanied by four endothermic peaks, corresponding to the dehydration (118 °C, stage A), initial decomposition of the nitrate groups (145 °C, stage B), full decomposition of the nitrate groups (208 °C, stage C) and the deoxidation of CuO into Cu_2O (261 °C, stage D) that would oxidize some of the glucose-produced carbon. However, when the decomposition of $Cu(NO_3)_2{\cdot}3H_2O$ is performed in H_2 gas atmosphere

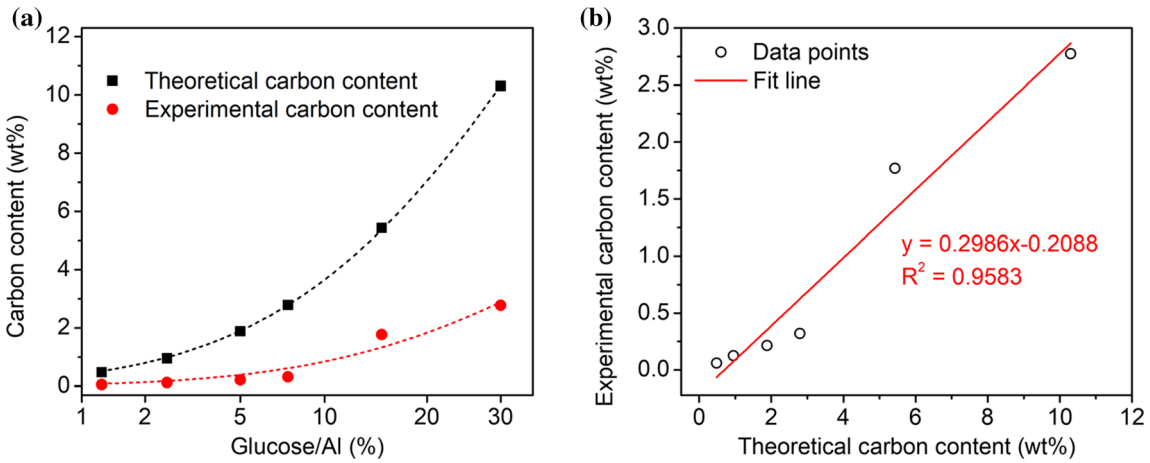

Figure 3 **a** Experimental and theoretical contents *vs* the initial glucose/Al mass ratio. **b** Experimental carbon content *vs* theoretical carbon content. The fit lines are guides to the eye.

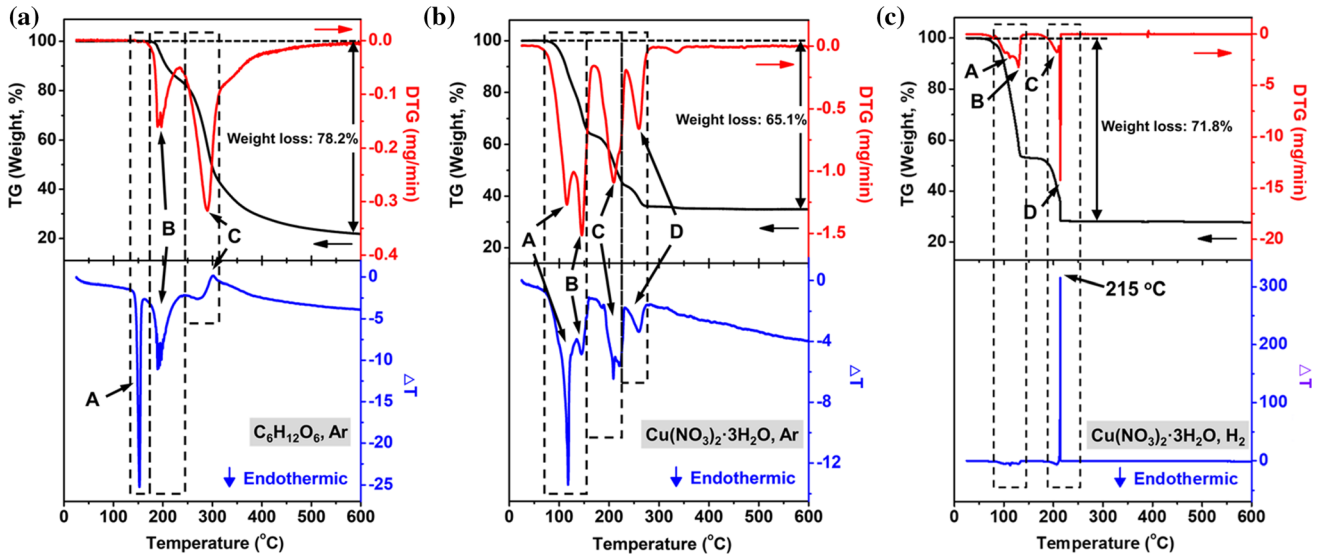

Figure 4 TG (black), DTG (red) and DTA (blue) curves for **a** $C_6H_{12}O_6$ in Ar gas atmosphere, **b** $Cu(NO_3)_2{\cdot}3H_2O$ in Ar gas atmosphere and **c** $Cu(NO_3)_2{\cdot}3H_2O$ in H_2 gas atmosphere.

(Fig. 4c), as for sample S0R, Cu_2O is reduced to metallic Cu and this is accompanied by an intense exothermic peak at 215 °C.

Analysis of the XRD patterns of the S0R and S0C–S6C powders (Fig. 5a) reveals five main diffraction peaks corresponding to Al. In addition to them, as shown in Fig. 5b, two peaks corresponding to Cu were detected for S0R while a group of peaks corresponding to Al_2Cu was detected for S0C. For S1C–S6C, two Cu peaks were detected, the intensity of which is constant for S1C–S4C and increases for S5C and S6C. Peaks of weak intensity attributed to Al_2Cu are detected for S1C, S2C and S3C, with a progressively decreasing intensity, and no more present for S4C–S6C. This could indicate that for the former samples, with a low carbon content, the Cu particles were dissolved into the Al matrix and precipitated in the form of Al_2Cu nanoparticles upon cooling [43, 44], whereas for the latter samples, containing a higher carbon content, the formation of GNS around the Cu particles would have prevented their dissolution in the first place.

The Raman spectra of S3C–S6C (Fig. 6) reveal the carbon D-band ($\sim$ 1350 cm^{-1}) and the G-band ($\sim$ 1590 cm^{-1}) while they are not detected of those of S1C and S2C (not shown). Although it is difficult to precisely determine on the present spectra, the I_D/I_G value seems to increase upon the increase in carbon

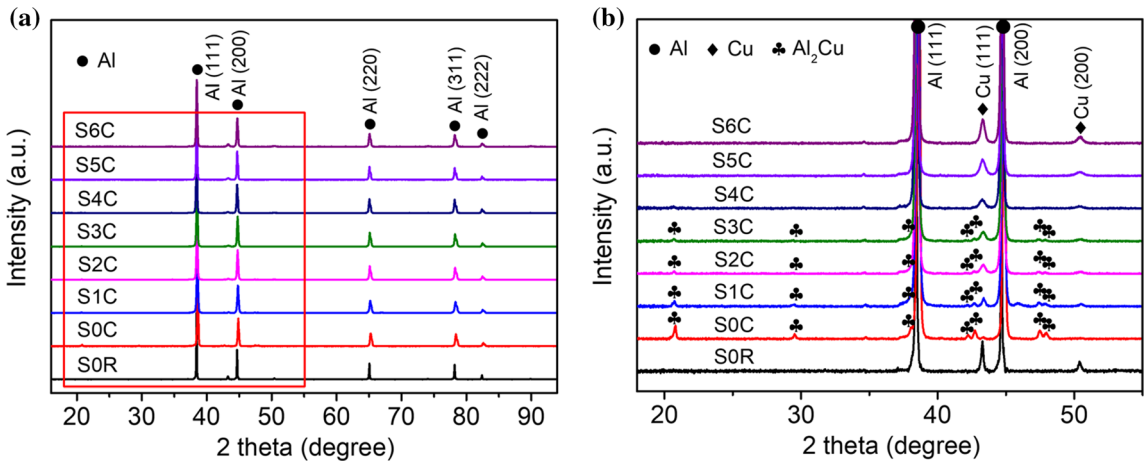

Figure 5 **a** XRD patterns of the GNS Cu/Al composite powders and **b** enlarged details corresponding to the boxed area in (**a**).

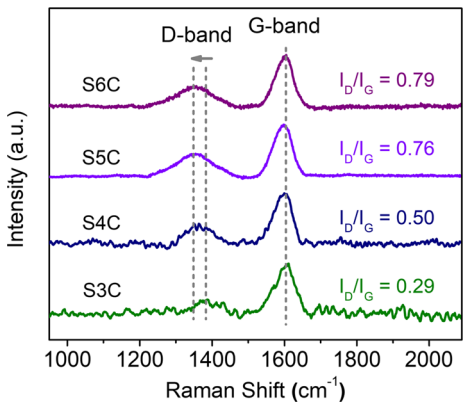

Figure 6 Raman spectra of the S3C S6C GNS Cu/Al composite powders.

content, from 0.29 for S3C (0.22 wt.%) to 0.79 for S6C (2.78 wt.%). These values are close to those reported for graphene samples obtained using a similar synthesis method [36, 38]. These increasing I_D/I_G ratios reflect higher disorder and defects [45] associated with the increasing number of graphene layers and the increased non-planar nature of the GNS surrounding the Cu particles at the high GNS contents.

SEM images (BSE mode) of the S1C–S6C powders (Fig. 7) reveal that the surface of the Al particles is partially covered by nanosized particles which are uniformly distributed as disordered clusters in some transparent encapsulating layers (dashed boxes in Fig. 7). Meanwhile, these encapsulating layers are tightly attached on the surfaces of Al powders. It is supposed that such layers are formed by the simultaneous decomposition of glucose and copper nitrate, which would therefore consist of GNS–Cu hybrids. Moreover, for S1C (Fig. 7a) and S2C (Fig. 7b), significantly larger particles (100–200 nm) are observed, which could correspond to the Al_2Cu particles detected by XRD (Fig. 5). It is possible that such particles were not observed for S3C because of their limited amount. Additionally, with the increase in the carbon content, the morphology of the hybrid layers gradually transforms from separated fragments to complete sheets.

To further characterize the GNS–Cu hybrid layers, a part of the S3C sample was sonicated in anhydrous ethanol for 30 min in order to separate them from the Al grains. The so-obtained suspension was dropped on a perforated carbon film covering a copper grid for TEM observation (Fig. 8). A BF-STEM image (Fig. 8a) and the corresponding EDS mapping (Fig. 8b, c) reveal that a GNS–Cu hybrid layer is made up of a transparent GNS layer decorated with Cu nanoparticles with a diameter equal to 45 ± 7 nm (Fig. 8d). Higher-magnification images (Fig. 8e, f) reveal different areas where the GNS layer bridges adjacent Cu particles. Moreover, an HRTEM image (Fig. 8g) shows GNS formed around the Cu particle in the layer, evidencing their intimate bonding [26]. An inverse fast Fourier transform (IFFT) image (Fig. 8h) shows the (002) planes of GNS (interplanar spacing 0.34 nm) and the (111) Cu planes (interplanar spacing 0.21 nm).

Clearly, the interaction of GNS, originating from the decomposition of glucose, with the Cu particles, originating from the decomposition of copper nitrate, hampered the growth of the Cu particles. For the sake of comparison, powder S0R prepared by H_2 reduction at 300 °C was also observed (Fig. 9). SEM images (BSE mode) show that the Al grains are not sintered

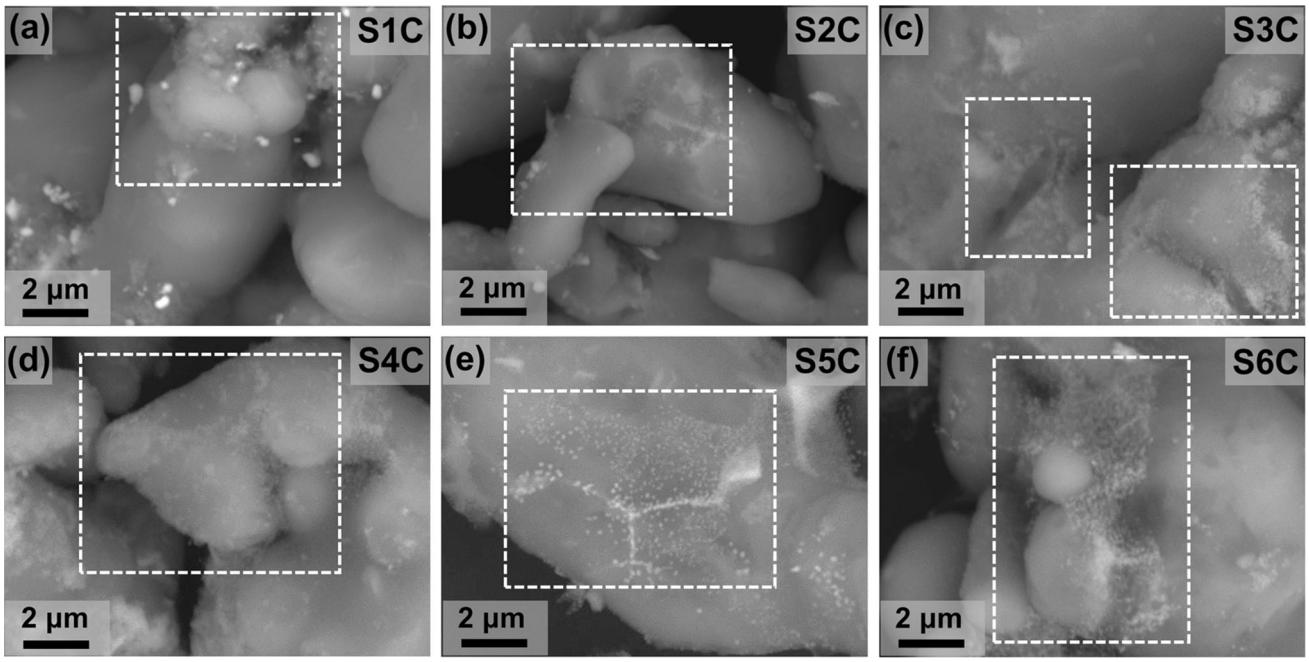

Figure 7 SEM images (BSE mode) of the S1C S6C GNS Cu/Al composite powders. The boxed areas indicate some GNS Cu hybrid layers.

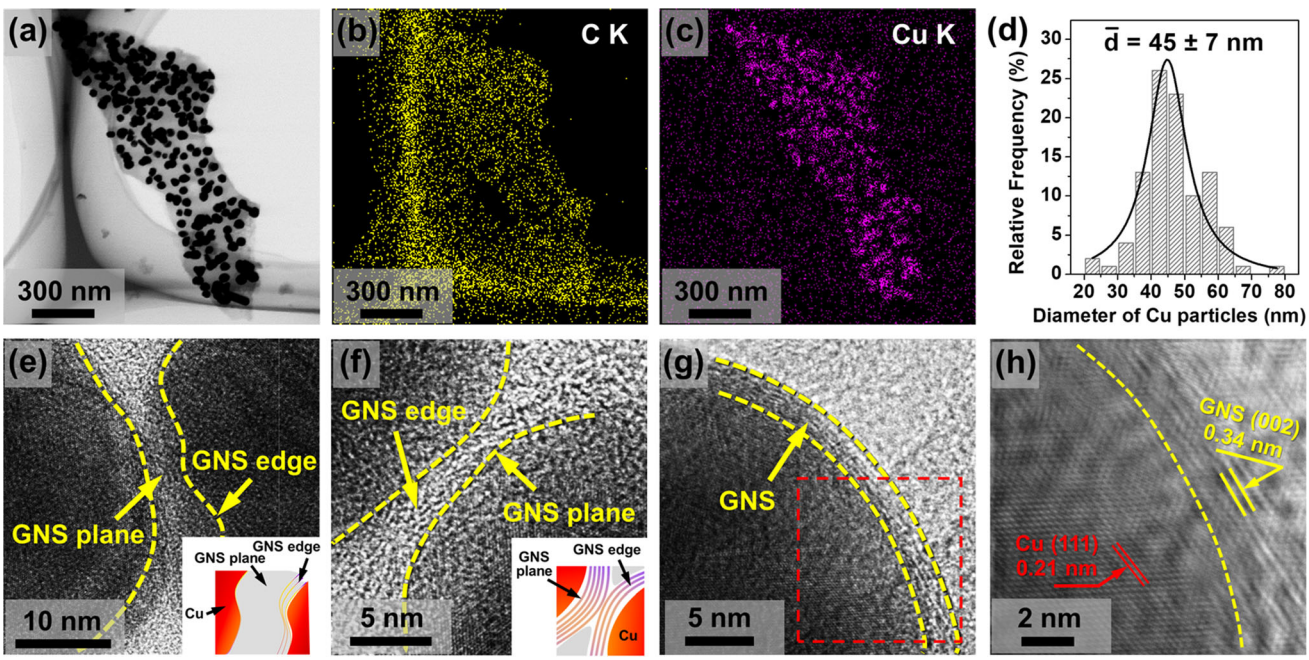

Figure 8 **a** BF STEM image of a GNS Cu hybrid layer and **b**, **c** the corresponding EDS mapping; **d** the Cu particles diameter distribution. **e**, **f** HRTEM images showing the GNS layer bridging adjacent Cu particles, **g** HRTEM images showing a GNS surrounding a Cu particle and **h** the IFFT image of the boxed area box in (**g**).

(Fig. 9a) and that the Cu particles located on their surface (bright contrast in Fig. 9b) have a diameter of 269 ± 63 nm (Fig. 9c), which is much bigger than those located in the hybrid layer (45 nm, Fig. 8d).

To summarize this section, three kinds of GNS–Cu/Al composite powders have been synthesized: (i) S1C and S2C containing Cu, precipitated Al_2Cu but without detectable GNS; (ii) S3C containing Cu,

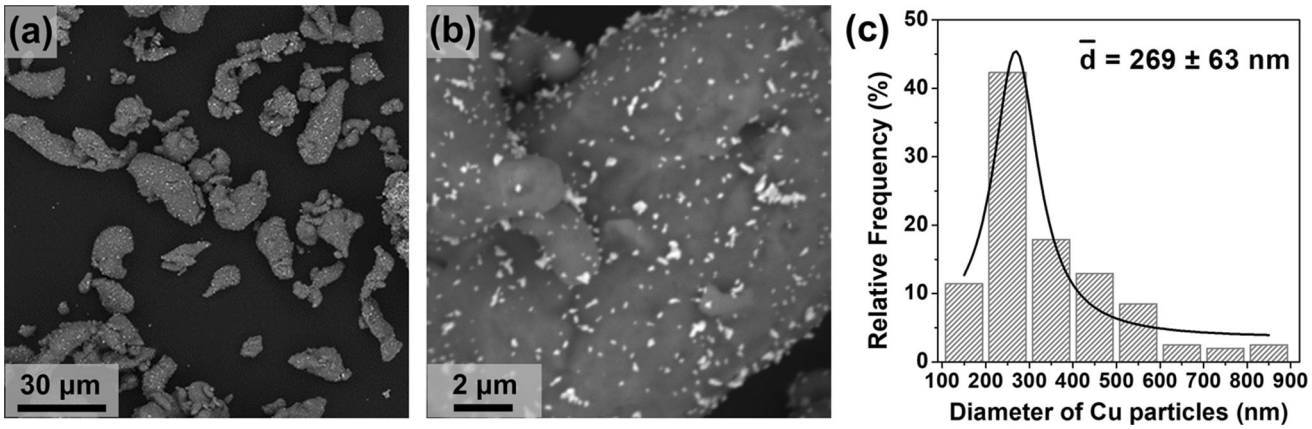

Figure 9 **a**, **b** SEM images (BSE mode) of the S0R Cu/Al composite powder; **c** diameter distribution of the Cu particles located at the surface of the Al grains.

less precipitated Al_2Cu and GNS–Cu hybrid layers and (iii) S4C, S5C and S6C containing Cu, GNS–Cu hybrid layers and no Al_2Cu. The S3C and S5C, as well as carbon-free Cu/Al powder (S0R), were selected for the rest of the study.

Sintered samples

The relative density of the S0R and S3C samples sintered under S-4-4 and S-5-1 conditions are similar (about 99.6%, see Table 2). It is slightly lower for the corresponding S5C samples (about 98.6%, see Table 2), which could reflect the higher carbon content in the S5C samples, the sintering being hampered by the GNS layers surrounding the Al grains.

Analysis of the XRD patterns of S-4-4 samples (Fig. 10a) shows that Al_2Cu is faintly detected in S3CS-4-4 but not for S0RS-4-4 and S5CS-4-4, for which a strong Cu (111) peak is accordingly detected. By contrast, Al_2Cu peaks are present for all XRD patterns of three S-5-1 samples (Fig. 10b). Compared to the patterns recorded for the corresponding powders (Fig. 5b), S3C does not change much whatever the sintering conditions, probably because of the presence of the GNS–Cu hybrid layer. For S5C, the Cu particles probably only grow slightly under the S-4-4 conditions whereas they react with Al to form Al_2Cu under the S-5-1 conditions.

S3CS-4-4 was investigated by TEM (Fig. 11). As shown in Fig. 11a, the GNS–Cu hybrid layers are dispersed crossing the matrix grain boundary, presenting intact interfaces (yellow dashed line) along with a high density of dislocations in the Al grain interior (white arrow). The HAADF-STEM image (Fig. 11b) and the corresponding EDS element maps (Fig. 11c–e) reveal that the copper element (Fig. 11d) is mostly located at the grain boundaries of the Al matrix and as small particles within the Al grains (white arrows in Fig. 11b), which could correspond to the Al_2Cu particles formed by precipitation while still in the powder state. Interestingly, carbon (Fig. 11e) is detected very homogenously over the area, which could account for the GNS–Cu hybrid layers covering the Al grain. Such hybrid layers could also be

Table 2 Carbon content, SPS maximum temperature (T_{SPS}), SPS maximum uniaxial pressure (P_{SPS}), density and relative density for the S0R, S3C and S5C sintered samples

Sample	Carbon content (wt%)	T_{SPS} (°C)	P_{SPS} (MPa)	Density (g/cm^3)	Relative density (%)
S0RS 4 4	0	400	400	2.77 ± 0.01	99.5 ± 0.4
S0RS 5 1	0	500	100	2.78 ± 0.04	99.6 ± 1.3
S3CS 4 4	0.22	400	400	2.78 ± 0.02	99.7 ± 0.7
S3CS 5 1	0.22	500	100	2.77 ± 0.01	99.6 ± 0.4
S5CS 4 4	1.77	400	400	2.73 ± 0.01	98.5 ± 0.5
S5CS 5 1	1.77	500	100	2.74 ± 0.01	98.6 ± 0.5

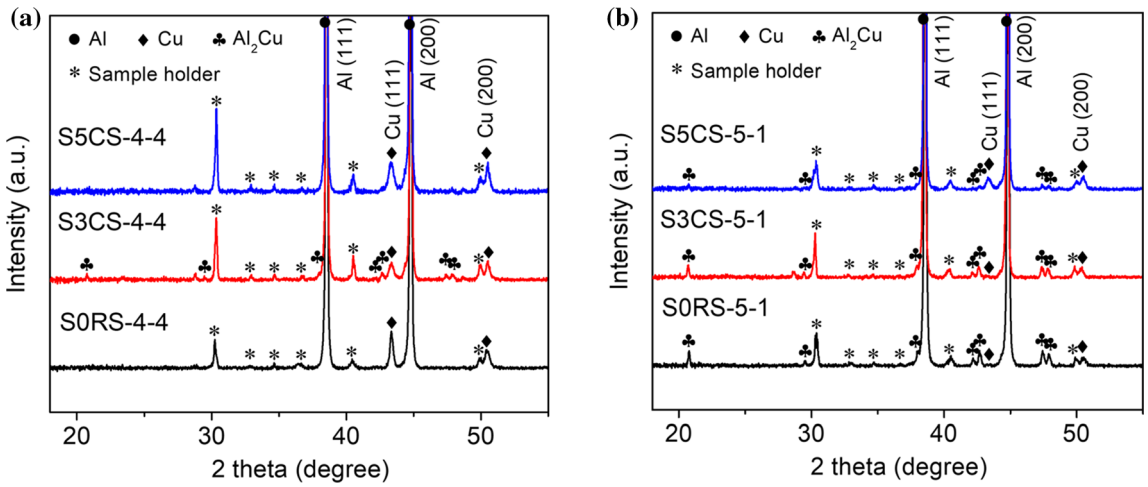

Figure 10 XRD patterns of the S0R, S3C and S5C samples sintered in the conditions of **a** S 4 4 and **b** S 5 1. See text for details.

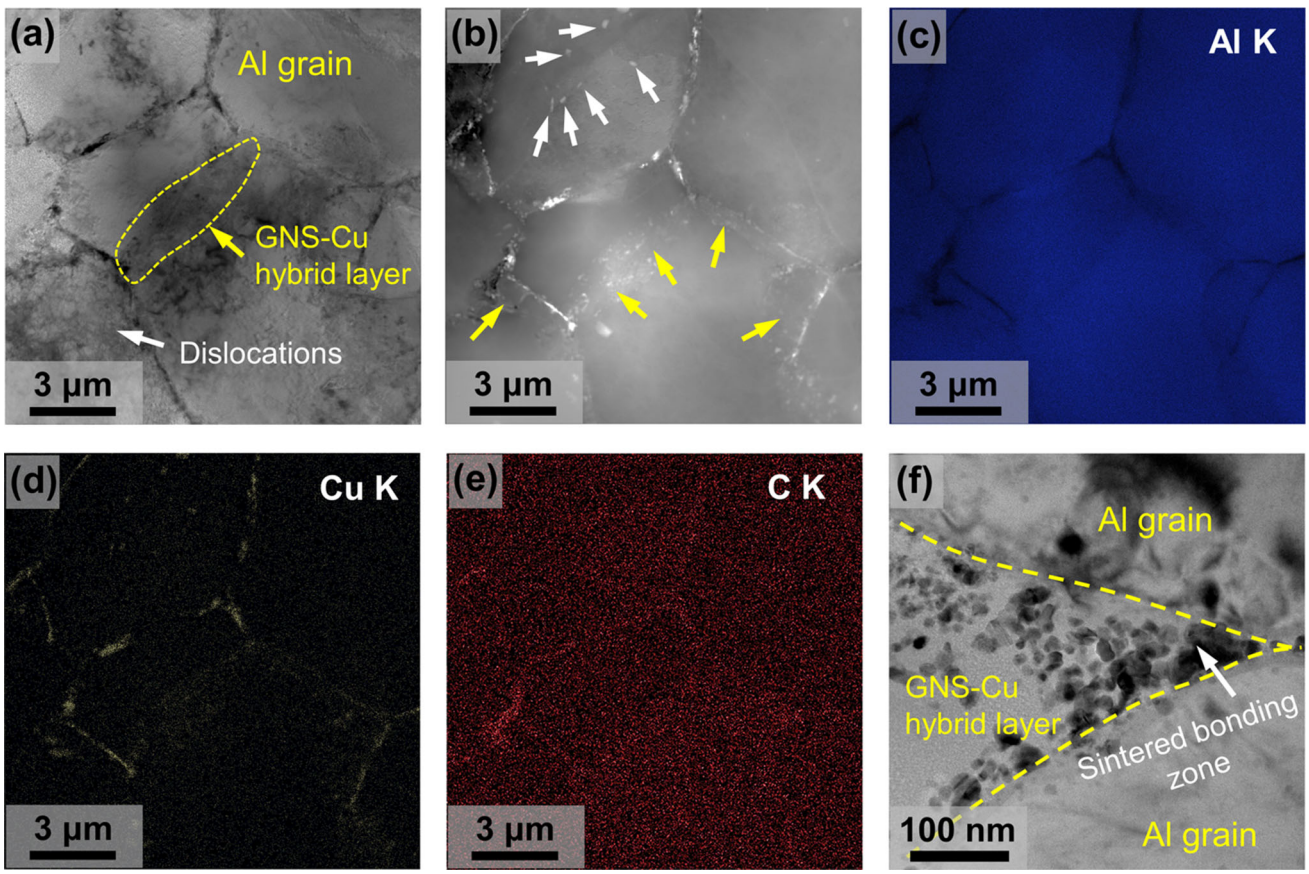

Figure 11 **a** TEM image, **b** HAADF STEM image and **c** **e** the corresponding EDS element maps of GNS Cu/Al sintered composite S3CS 4 4; **f** TEM image showing an area of the interface between the GNS Cu hybrid layers and Al grains.

observed on the HAADF-STEM image (yellow arrows in Fig. 11b). A TEM image (Fig. 11f) shows an area of the interface between the GNS–Cu hybrid layers and Al grains, where the flexible GNS layers are connected to each other after SPS, through the exposed Cu nanoparticles (yellow arrows in Fig. 11f). Therefore, in such a "sintered bonding zone," two non-coplanar GNS layers have become strongly bonded. Some earlier studies [35, 36, 43] reveal that such bonding is strengthened by the lock-in of

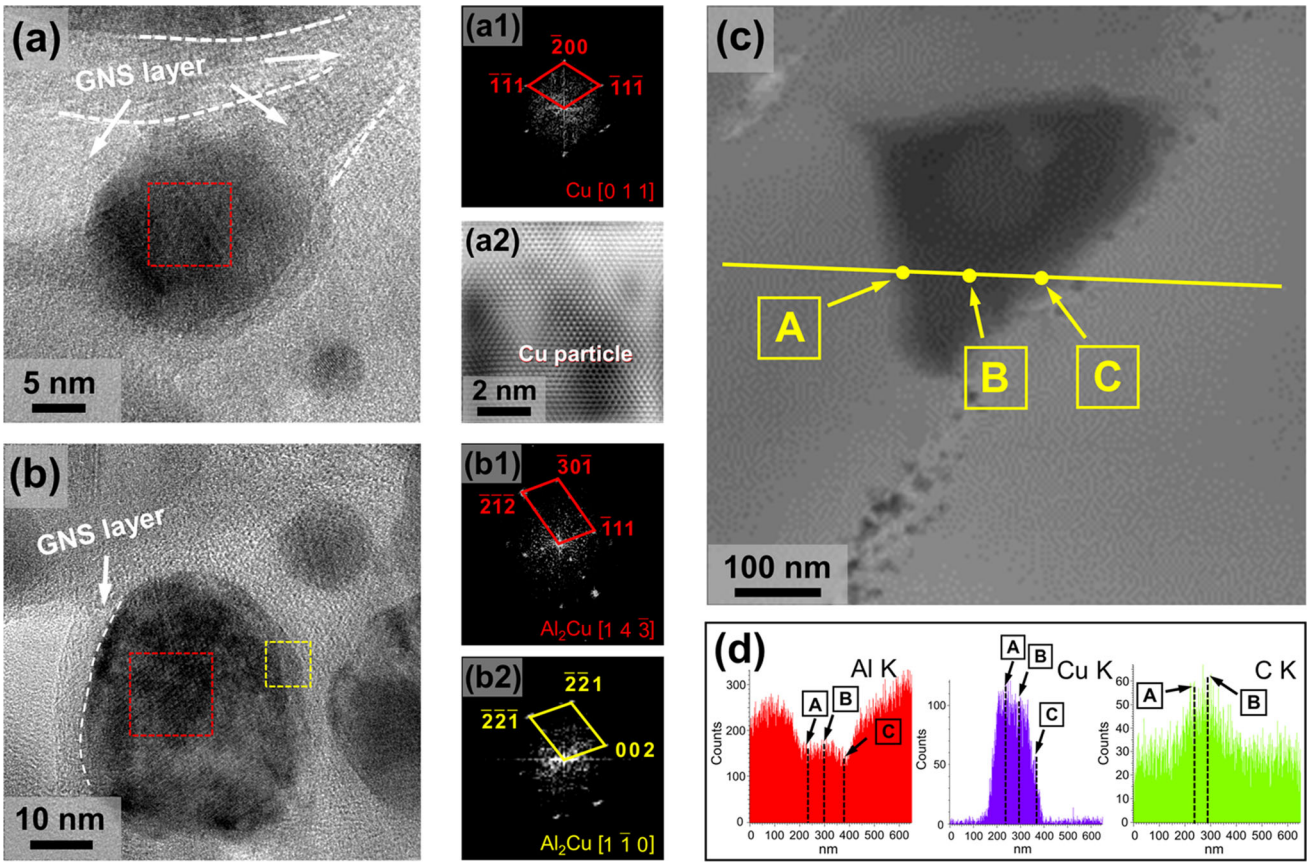

Figure 12 **a**, **b** HRTEM images and the corresponding (a1, b1, b2) FFT images and (a2) IFFT images of the GNS Cu/Al sintered composite S3CS 5 1; **c** BF STEM image and **d** EDS line scanning results along the yellow line in (**c**) for the distribution of Al, Cu and C elements.

intermetallic compounds at the interface. Compared to those earlier studies, the one-step synthesis method in this study undoubtedly enables a more uniform interface area, hence offering much potential for tuning the morphology of interfacial metal nanoparticles.

The S3CS-5-1 sample was also observed by TEM (Fig. 12). A spherical nanoparticle (~ 20 nm) completely encapsulated by GNS layers was verified as pure Cu by combining HRTEM with FFT/IFFT (Fig. 12a, a1 and a2). An irregular nanoparticle with a larger size (~ 40 nm) was observed with a thin and incomplete GNS encapsulating shell (Fig. 12b). A study of the FFT patterns (Fig. 12b1, b2) corresponding to the central and edge areas (red and yellow boxes, respectively, in Fig. 12b) of the particle reveals that the particle is Al_2Cu. A large irregular particle (~ 200 nm) located at the grain boundary was also investigated (Fig. 12c). To unveil the element distribution within this irregular particle, an EDS line scan was performed (yellow line in Fig. 12c). The distribution of Al element presents a kind of "double-valley" shape (ranging from position A to position C, Fig. 12d). Starting from the left, the transition from the matrix to the particle (noted as A in Fig. 12c) marks a minimum in Al concentration. It increases up to the middle of the particle (noted as B in Fig. 12c) and decreases again down to the other edge (noted as C in Fig. 12c). This reveals that Al atoms diffused into the particle interior. Intriguingly, the Cu and carbon elements show a bimodal distribution with peak values at the same A and B positions (Fig. 12d), which could reflect that the surface of this irregular particle is enriched in copper and carbon. In addition, there clearly is a Cu concentration gradient with the particle, and for position C, the value of Cu/Al atomic ratio is nearly 0.5, corresponding to the Al_2Cu phase. The Al–Cu element distribution within this irregular particle suggests a

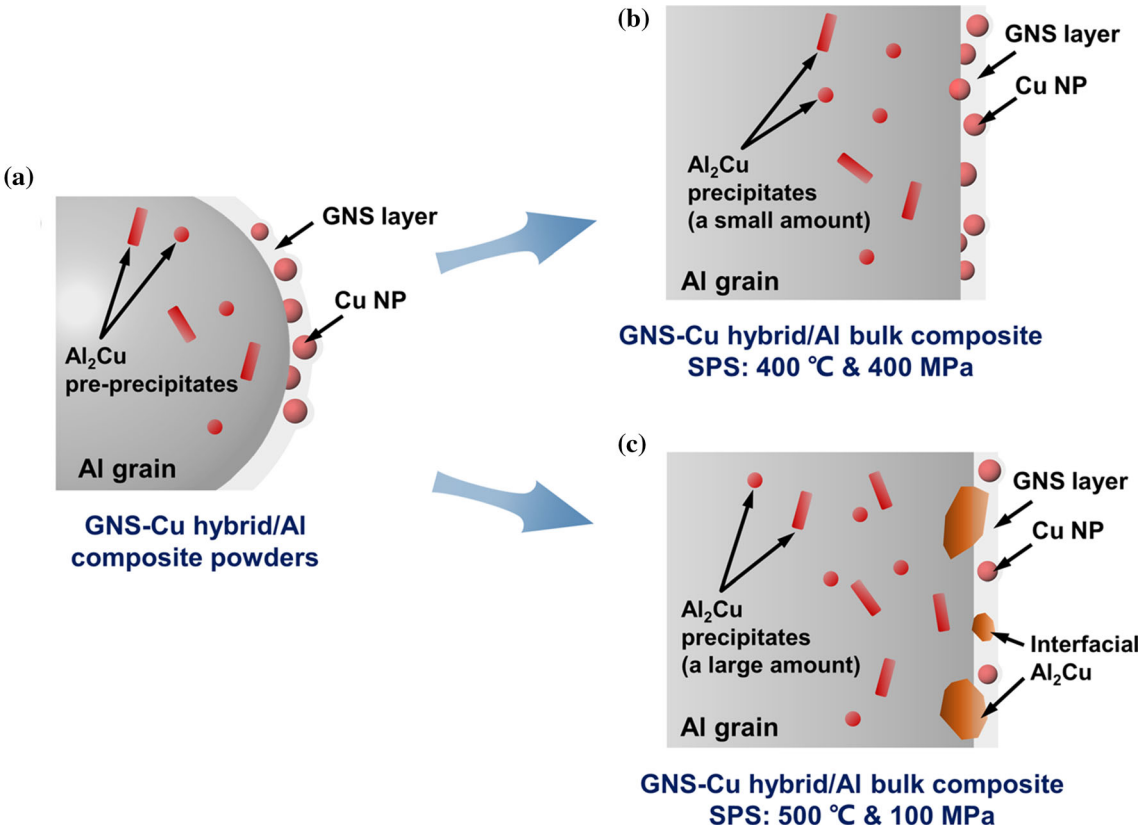

Figure 13 Schematic diagram of composition and microstructure for **a** the GNS Cu/Al composite powder, **b** the sample sintered in the S 4 4 conditions and **c** the sample sintered in the S 5 1 conditions.

formation mechanism of interfacial precipitates dominated by elemental interdiffusion [46].

The in situ synthesized GNS–Cu/Al composite powder S3C was sintered using two different SPS conditions (S-4-4 and S-5-1) and the evolution of the composition and microstructure, as deduced from the results presented above, is summarized in Fig. 13.

In the powders (Fig. 13a), a GNS–Cu hybrid layer is formed and attached to the surface of the Al grains. Generally, Cu elements with the content below 5 wt% after solid-solution treatment can fully dissolve in the Al matrix and afterward precipitate to form Al_2Cu [43]. Because of the calcination step at 600 °C, a part of Cu atoms was dissolved in the Al grains and precipitated as Al_2Cu during cooling. Those dissolved Cu atoms are preferentially precipitated in grain interiors along the position of coherent interface with the Al matrix [47], thereby some Al_2Cu phases show needlelike morphology (white arrows in Fig. 11b). Upon sintering in the S-4-4 conditions (Fig. 13b), there is also a limited intragranular precipitation of Al_2Cu but not at the surface of the Al grains, where a continuous GNS–Cu hybrid layer is located at the grain boundaries. By contrast, upon sintering in the S-5-1 conditions (Fig. 13c), firstly, intragranular Al_2Cu precipitation is more widespread and secondly, those Cu nanoparticles only partially covered by the GNS reacted with Al matrix to form Al_2Cu particles located at the grain boundaries.

Microhardness and elastic modulus

The Vickers microhardness (HV) of samples S0R, S3C and S5C are shown in Fig. 14a and Table 3. For the samples sintered in the S-4-4 conditions, the microhardness increases from S0R (54 HV) to S3C (75 HV), which could reflect the presence of the GNS–Cu hybrid layers, but decreases for S5C (54 HV), which could reflect the decrease in densification. Notably, for the samples sintered in the S-5-1 conditions, the evolution is similar but the microhardness values are

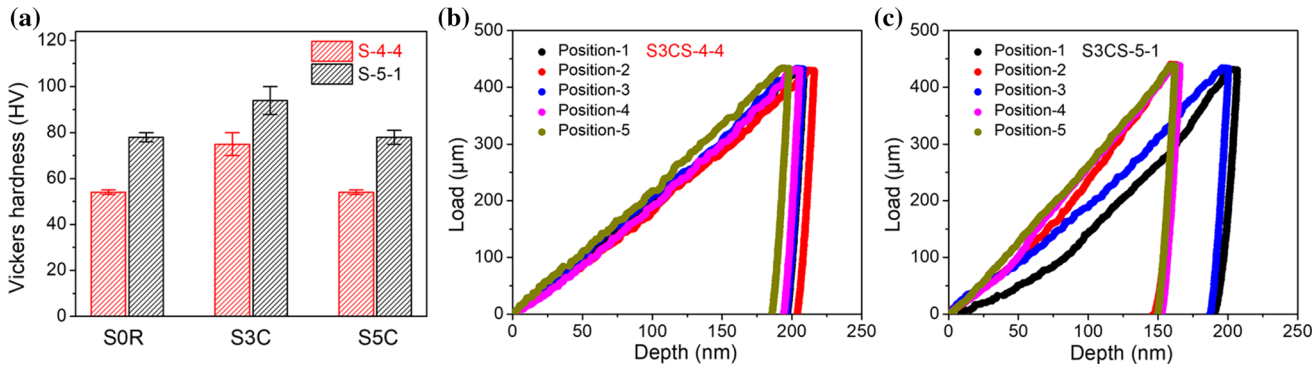

Figure 14 **a** Vickers microhardness (HV) for the S0R, S3C and S5C samples sintered in the S 4 4 and S 5 1 conditions; nanoindentation load depth curves for **b** S3CS 4 4 and **c** S3CS 5 1.

Table 3 Microhardness (HV) and elastic modulus, the latter derived from nanoindentation tests, for the S0R, S3C and S5C samples sintered in the S 4 4 and S 5 1 conditions. See text for details

Sample	Relative density (%)	Microhardness (HV)	Elastic modulus (GPa)
S0RS 4 4	99.5 ± 0.4	54 ± 1	
S0RS 5 1	99.6 ± 1.3	78 ± 2	
S3CS 4 4	99.7 ± 0.7	75 ± 5	74.8 ± 1.7
S3CS 5 1	99.6 ± 0.4	94 ± 6	83.3 ± 6.6
S5CS 4 4	98.5 ± 0.5	54 ± 1	
S5CS 5 1	98.6 ± 0.5	78 ± 3	

significantly higher (78, 94 and 78 HV, respectively). In order to understand this evolution, nanoindentation tests were carried out for S3CS-4-4 and S3CS-5-1, on five different positions inside the grains and near the interfaces. The load–depth curves for all the positions for S3CS-4-4 (Fig. 14b) exhibit a good consistency, while some positions for S3CS-5-1 (Fig. 14c) show a lower indentation depth, indicating higher values of the local hardness and elastic modulus (Table 3). The higher microhardness of S3CS-5-1 compared to S3CS-4-4 can be ascribed to two factors. For one thing, the higher microhardness could reflect the formation of Al_2Cu, either inside the Al grains (Fig. 11b) or at the interface (Fig. 12c). The formation of Al_4C_3 was also reported to provide a similar effect on the hardening of graphene–Al composites [20]. However, as compared with Al_4C_3 which was easily produced at the defect site, the formation of Al_2Cu [36] or Al_3Ni [22] through the reaction of the Al grains with the modified particles of GNSs would not consume the carbon components, so that the structural integrity of GNSs could be maintained well. For another thing, a large amount of in situ formed Al_2Cu as well as GNS–Cu hybrid layers would play crucial roles in serving as effective barriers to dislocation motion, thus hardening the Al matrix [48, 49].

Conclusions

A novel GNS-Cu hybrid was in situ synthesized as layers on Al grains by a one-step decomposition of freeze-dried glucose/copper nitrate gel precursors. It is shown that the Cu nanoparticles, which catalyzed the nucleation and growth of GNS from glucose decomposition, end up as particles about 45 nm in size uniformly dispersed in GNS-Cu hybrid layers wrapping part of the Al grains. Intragranular Al_2Cu is formed by precipitation albeit in a limited amount. The GNS-Cu/Al composites were consolidated by SPS using 400 °C/400 MPa or 500 °C/100 MPa conditions. It is shown that the latter conditions favor intragranular Al_2Cu precipitation, and also most importantly, the formation of Al_2Cu particles located at the grain boundaries by reaction of the Cu nanoparticles only partially covered by the GNS with the Al matrix. Such particles provide increased bonding between the GNS and the matrix, and improve the strength in the area near interfaces of composite with the increase in them. It is demonstrated that the significantly higher microhardness and elastic modulus (94 HV and 83.3 GPa, respectively) were achieved in bulk composites under the SPS condition of 500 °C/100 MPa, provided the

carbon (in the form of GNS) content is kept low enough in order to avoid hampering the densification. The present findings provide new guidance for elucidating the evolutions and roles of metal-decorated graphene hybrids in Al matrix composites.

Acknowledgements

The work was supported by the China Scholarship Council and the Equipment Advance Research Fund (No. 61409220102) and by the Teaching and Large-scale Instrument Experiment Center, School of Materials Science and Engineering, Tianjin University. The support of the Plateforme Nationale CNRS de Frittage Flash (PNF^2/CNRS) at Université Toulouse 3 Paul Sabatier is gratefully appreciated.

Author contributions

BP contributed to the experiment, characterization and writing of the original draft. DM was involved in the analysis and revising. CE contributed to resources and revising. XZ was involved in the analysis and investigation. GC was involved in the experiment and investigation. NZ contributed to validation and project administration. CL was involved in the supervision, project administration and revising.

Declaration

Competing interest The authors declare that they have no known competing financial interests or personal relationships that could have appeared to influence the work reported in this paper.

References

[1] Geim AK, Novoselov KS (2007) The rise of Graphene. Nat Mater 6:183 191. https://doi.org/10.1038/nmat1849

[2] Stankovich S, Dikin DA, Dommett GHB et al (2006) Graphene based composite materials. Nature 442:282 286. https://doi.org/10.1038/nature04969

[3] Nieto A, Bisht A, Lahiri D, Zhang C, Agarwal A (2016) Graphene reinforced metal and ceramic matrix composites: a review. Int Mater Rev 62:241 302. https://doi.org/10.1080/09506608.2016.1219481

[4] Tjong SC (2013) Recent progress in the development and properties of novel metal matrix nanocomposites reinforced with carbon nanotubes and graphene nanosheets. Mater Sci Eng, R 74:281 350. https://doi.org/10.1016/j.mser.2013.08.001

[5] Wang JY, Li ZQ, Fan GL, Pan HH, Chen ZX, Zhang D (2012) Reinforcement with graphene nanosheets in aluminum matrix composites. Scr Mater 66:594 597. https://doi.org/10.1016/j.scriptamat.2012.01.012

[6] Gao X, Yue HY, Guo EJ, Zhang H, Lin XY, Yao LH, Wang B (2016) Preparation and tensile properties of homogeneously dispersed graphene reinforced aluminum matrix composites. Mater Des 94:54 60. https://doi.org/10.1016/j.matdes.2016.01.034

[7] Li Z, Fan GL, Tan ZQ, Guo Q, Xiong DB, Su YS, Li ZQ, Zhang D (2014) Uniform dispersion of graphene oxide in aluminum powder by direct electrostatic adsorption for fabrication of graphene/aluminum composites. Nanotechnology 25:325601. https://doi.org/10.1088/0957 4484/25/32/325601

[8] Liu JH, Khan U, Coleman J, Fernandez B, Rodriguez P, Naher S, Brabazon D (2016) Graphene oxide and graphene nanosheet reinforced aluminium matrix composites: Powder synthesis and prepared composite characteristics. Mater Des 94:87 94. https://doi.org/10.1016/j.matdes.2016.01.031

[9] Ju J M, Wang GF, Sim K H (2017) Facile synthesis of graphene reinforced Al matrix composites with improved dispersion of graphene and enhanced mechanical properties. J Alloy Compd 704:585 592. https://doi.org/10.1016/j.jallcom.2017.01.314

[10] Jiang YY, Tan ZQ, Xu R et al (2018) Tailoring the structure and mechanical properties of graphene nanosheet/aluminum composites by flake powder metallurgy via shift speed ball milling. Compos Part A Appl Sci 111:73 82. https://doi.org/10.1016/j.compositesa.2018.05.022

[11] Li Z, Guo Q, Li Z, Fan G, Xiong DB, Su Y, Zhang J, Zhang D (2015) Enhanced mechanical properties of graphene (reduced graphene oxide)/aluminum composites with a bioinspired nanolaminated structure. Nano Lett 15:8077 8083. https://doi.org/10.1021/acs.nanolett.5b03492

[12] Zhang ZW, Liu ZY, Xiao BL, Ni DR, Ma ZY (2018) High efficiency dispersal and strengthening of graphene reinforced aluminum alloy composites fabricated by powder metallurgy combined with friction stir processing. Carbon 135:215 223. https://doi.org/10.1016/j.carbon.2018.04.029

[13] Huang Y, Bazarnik P, Wan DQ et al (2019) The fabrication of graphene reinforced Al based nanocomposites using high pressure torsion. Acta Mater 164:499 511. https://doi.org/10.1016/j.actamat.2018.10.060

[14] Li JC, Zhang XX, Geng L (2018) Improving graphene distribution and mechanical properties of GNP/Al composites

by cold drawing. Mater Des 144:159 168. https://doi.org/10.1016/j.matdes.2018.02.024

[15] Pu BW, Zhang X, Zhao DD, He CN, Shi CS, Liu EZ, Sha JW, Zhao NQ (2021) Achieving prominent strengthening efficiency of graphene nanosheets in Al matrix composites by hybrid deformation. Carbon 183:530 545. https://doi.org/10.1016/j.carbon.2021.07.042

[16] Ju BY, Yang WS, Shao PZ et al (2020) Effect of interfacial microstructure on the mechanical properties of GNPs/Al composites. Carbon 162:346 355. https://doi.org/10.1016/j.carbon.2020.02.069

[17] Zhang HP, Xu C, Xiao WL, Ameyama K, Ma CL (2016) Enhanced mechanical properties of Al5083 alloy with graphene nanoplates prepared by ball milling and hot extrusion. Mater Sci Eng, A 658:8 15. https://doi.org/10.1016/j.msea.2016.01.076

[18] Zhou WW, Yamaguchi T, Kikuchi K, Nomura N, Kawasaki A (2017) Effectively enhanced load transfer by interfacial reactions in multi walled carbon nanotube reinforced Al matrix composites. Acta Mater 125:369 376. https://doi.org/10.1016/j.actamat.2016.12.022

[19] Zhou WW, Mikulova P, Fan YC, Kikuchi K, Nomura N, Kawasaki A (2019) Interfacial reaction induced efficient load transfer in few layer graphene reinforced Al matrix composites for high performance conductor. Compos Part B Eng 167:93 99. https://doi.org/10.1016/j.compositesb.2018.12.018

[20] Zhou WW, Dong MQ, Zhou ZX, Sun XH, Kikuchi K, Nomura N, Kawasaki A (2018) In situ formation of uniformly dispersed Al_4C_3 nanorods during additive manufacturing of graphene oxide/Al mixed powders. Carbon 141:67 75. https://doi.org/10.1016/j.carbon.2018.09.057

[21] Chen B, Shen J, Ye X, Imai H, Umeda J, Takahashi M, Kondoh K (2017) Solid state interfacial reaction and load transfer efficiency in carbon nanotubes (CNTs) reinforced aluminum matrix composites. Carbon 114:198 208. https://doi.org/10.1016/j.carbon.2016.12.013

[22] Guan R, Wang Y, Zheng S, Su N, Ji Z, Liu Z, An Y, Chen B (2019) Fabrication of aluminum matrix composites reinforced with Ni coated graphene nanosheets. Mater Sci Eng, A 754:437 446. https://doi.org/10.1016/j.msea.2019.03.068

[23] Guan C, Zhao YT, Chen G et al (2021) Synergistic strengthening and toughening of copper coated graphene nanoplates and in situ nanoparticles reinforced AA6111 composites. Mater Sci Eng, A 822:141661. https://doi.org/10.1016/j.msea.2021.141661

[24] Zhang ZM, Fan GL, Tan ZQ, Zhao HT, Xu YJ, Xiong DB, Li ZQ (2021) Bioinspired multiscale Al_2O_3 rGO/Al laminated composites with superior mechanical properties. Compos Part B Eng 217:108916. https://doi.org/10.1016/j.compositesb.2021.108916

[25] Zhang X, Li H, Ding F (2014) Self assembly of carbon atoms on transition metal surfaces chemical vapor deposition growth mechanism of graphene. Adv Mater 26:5488 5495. https://doi.org/10.1002/adma.201305922

[26] Zhang X, Shi CS, Liu EZ, Zhao NQ, He CN (2018) Effect of interface structure on the mechanical properties of graphene nanosheets reinforced copper matrix composites. ACS Appl Mater Inter 10:37586 37601. https://doi.org/10.1021/acsami.8b09799

[27] Yang Z, Wang L, Cui Y, Shi Z, Wang M, Fei W (2018) High strength and ductility of graphene like carbon nanosheet/copper composites fabricated directly from commercial oleic acid coated copper powders. Nanoscale 10:16990 16995. https://doi.org/10.1039/c8nr04451a

[28] He CN, Zhao NQ, Shi CS, Liu EZ, Li JJ (2015) Fabrication of nanocarbon composites using in situ chemical vapor deposition and their applications. Adv Mater 27:5422 5431. https://doi.org/10.1002/adma.201501493

[29] Li X, Cai W, Colombo L, Ruoff R (2009) Evolution of graphene growth on Ni and Cu by carbon isotope labeling. Nano Lett 9:4268 4272

[30] Weibel A, Mesguich D, Chevallier G, Flahaut E, Laurent C (2018) Fast and easy preparation of few layered graphene/magnesia powders for strong, hard and electrically conducting composites. Carbon 136:270 279. https://doi.org/10.1016/j.carbon.2018.04.085

[31] Weibel A, Flaureau A, Pham A, Chevallier G, Esvan J, Estournès C, Laurent C (2020) One step synthesis of few layered graphene/alumina powders for strong and tough composites with high electrical conductivity. J Eur Ceram Soc 40:5779 5789. https://doi.org/10.1016/j.jeurceramsoc.2020.06.029

[32] Cao M, Luo YZ, Xie YQ et al (2019) The influence of interface structure on the electrical conductivity of graphene embedded in aluminum matrix. Adv Mater Interfaces 6:1900468. https://doi.org/10.1002/admi.201900468

[33] Lee S, Hong J, Koo JH et al (2013) Synthesis of few layered graphene nanoballs with copper cores using solid carbon source. ACS Appl Mater Inter 5:2432 2437. https://doi.org/10.1021/am3024965

[34] Wang SL, Huang XL, He YH et al (2012) Synthesis, growth mechanism and thermal stability of copper nanoparticles encapsulated by multi layer graphene. Carbon 50:2119 2125. https://doi.org/10.1016/j.carbon.2011.12.063

[35] Liu G, Zhao NQ, Shi CS et al (2017) In situ synthesis of graphene decorated with nickel nanoparticles for fabricating reinforced 6061Al matrix composites. Mater Sci Eng, A 699:185 193. https://doi.org/10.1016/j.msea.2017.05.084

[36] Wang J, Zhang X, Zhao NQ, He CN (2018) In situ synthesis of copper modified graphene reinforced aluminum nanocomposites with balanced strength and ductility. J Mater Sci 54:5498 5512. https://doi.org/10.1007/s10853 018 032 45 2

[37] Qin J, He CN, Zhao NQ, Wang ZY, Shi CS, Liu EZ, Li JJ (2014) Graphene networks anchored with Sn@Graphene as Lithium Ion Battery Anode. ACS Nano 8:1728 1738

[38] Han TL, Liu EZ, Li JJ, Zhao NQ, He CN (2020) A bottom up strategy toward metal nano particles modified graphene nanoplates for fabricating aluminum matrix composites and interface study. J Mater Sci Technol 46:21 32. https://doi.org/10.1016/j.jmst.2019.09.045

[39] Pu BW, Sha JW, Liu EZ, He CN, Zhao NQ (2019) Synergistic effect of Cu on laminated graphene nanosheets/AlCu composites with enhanced mechanical properties. Mater Sci Eng, A 742:201 210. https://doi.org/10.1016/j.msea.2018.11.016

[40] Munir ZA, Anselmi Tamburini U, Ohyanagi M (2006) The effect of electric field and pressure on the synthesis and consolidation of materials: a review of the spark plasma sintering method. J Mater Sci 41:763 777. https://doi.org/10.1007/s10853 006 6555 2

[41] Chen B, Kondoh K, Imai H, Umeda J, Takahashi M (2016) Simultaneously enhancing strength and ductility of carbon nanotube/aluminum composites by improving bonding conditions. Scr Mater 113:158 162. https://doi.org/10.1016/j.scriptamat.2015.11.011

[42] Sun C, Zhang X, Zhao NQ, He CN (2019) Influence of spark plasma sintering temperature on the microstructure and strengthening mechanisms of discontinuous three dimensional graphene like network reinforced Cu matrix composites. Mater Sci Eng, A 756:82 91. https://doi.org/10.1016/j.msea.2019.04.032

[43] Zhao ZY, Guan RG, Guan XH, Feng ZX, Chen H, Chen Y (2015) Microstructures and properties of graphene Cu/Al composite prepared by a novel process through clad forming and improving wettability with copper. Adv Eng Mater 17:663 668. https://doi.org/10.1002/adem.201400173

[44] Nam DH, Cha SI, Lim BK, Park HM, Han DS, Hong SH (2012) Synergistic strengthening by load transfer mechanism and grain refinement of CNT/Al Cu composites. Carbon 50:2417 2423. https://doi.org/10.1016/j.carbon.2012.01.058

[45] Martins Ferreira EH, Moutinho MVO, Stavale F, Lucchese MM, Capaz RB, Achete CA, Jorio A (2010) Evolution of the Raman spectra from single , few , and many layer graphene with increasing disorder. Phys Rev B 82:125429. https://doi.org/10.1103/PhysRevB.82.125429

[46] Tavassoli S, Abbasi M, Tahavvori R (2016) Controlling of IMCs layers formation sequence, bond strength and electrical resistance in Al Cu bimetal compound casting process. Mater Des 108:343 353. https://doi.org/10.1016/j.matdes.2016.06.076

[47] Gao YH, Yang C, Zhang JY, Cao LF, Liu G, Sun J, Ma E (2018) Stabilizing nanoprecipitates in Al Cu alloys for creep resistance at 300°C. Mater Res Lett 7:18 25. https://doi.org/10.1080/21663831.2018.1546773

[48] Adlakha I, Garg P, Solanki KN (2019) Revealing the atomistic nature of dislocation precipitate interactions in Al Cu alloys. J Alloy Compd 797:325 333. https://doi.org/10.1016/j.jallcom.2019.05.110

[49] Shin SE, Bae DH (2015) Deformation behavior of aluminum alloy matrix composites reinforced with few layer graphene. Compos Part A Appl Sci 78:42 47. https://doi.org/10.1016/j.compositesa.2015.08.001